

PAPER

## Exploring the regime of validity of global gyrokinetic simulations with spherical tokamak plasmas

To cite this article: Y. Ren *et al* 2020 *Nucl. Fusion* **60** 026005

View the [article online](#) for updates and enhancements.



**IOP | ebooks™**

Bringing you innovative digital publishing with leading voices to create your essential collection of books in STEM research.

Start exploring the collection - download the first chapter of every title for free.

# Exploring the regime of validity of global gyrokinetic simulations with spherical tokamak plasmas

Y. Ren<sup>1,a</sup>, W.X. Wang<sup>1</sup>, W. Guttenfelder<sup>1</sup>, S.M. Kaye<sup>1</sup>, J. Ruiz-Ruiz<sup>2</sup>, S. Ethier<sup>1</sup>, R. Bell<sup>1</sup>, B.P. LeBlanc<sup>1</sup>, E. Mazzucato<sup>1</sup>, D.R. Smith<sup>3</sup>, C.W. Domier<sup>4</sup> and H. Yuh<sup>5</sup>

<sup>1</sup> Princeton Plasma Physics Laboratory, Princeton, NJ 08543, United States of America

<sup>2</sup> MIT-Plasma Science and Fusion Center, Cambridge, MA 02139, United States of America

<sup>3</sup> University of Wisconsin-Madison, Madison, WI, 53706, United States of America

<sup>4</sup> University of California at Davis, Davis, CA 95616, United States of America

<sup>5</sup> Nova Photonics, Inc., Princeton, NJ 08540, United States of America

E-mail: [yren@pppl.gov](mailto:yren@pppl.gov)

Received 15 July 2019, revised 19 November 2019

Accepted for publication 26 November 2019

Published 18 December 2019



CrossMark

## Abstract

Plasma turbulence is considered one of the main mechanisms for driving anomalous thermal transport in magnetic confinement fusion devices. Based on first-principle model, gradient-driven gyrokinetic simulations have often been used to explain turbulence-driven transport in present fusion devices, and in fact, many present predictive codes are based on the assumption that turbulence is gradient-driven. However, using the electrostatic global particle-in-cell gyrokinetic tokamak simulation (GTS) code (Wang *et al* 2010 *Phys. Plasmas* **17** 072511), we will show that while global gradient-driven gyrokinetic simulations provide decent agreement in ion thermal transport with a set of NBI-heated NSTX (Ono *et al* 2000 *Nucl. Fusion* **40** 557) H-mode plasmas, they are not able to explain the observed electron thermal transport variation in a set of RF-heated L-mode plasmas, where a factor of 2 decrease in electron heat flux is observed after the cessation of the RF heating. Thus, identifying the regime of validity of the gradient-driven assumption is essential for first-principle gyrokinetic simulation. This understanding will help us to more confidently predict the confinement performance of ITER and future magnetic confinement devices.

Keywords: turbulence, transport, tokamak, NSTX, electrostatic turbulence, gyrokinetic simulation, ion thermal transport

(Some figures may appear in colour only in the online journal)

## 1. Introduction

Micro-turbulence is considered to be a major candidate in driving anomalous transport in fusion plasmas [1]. The long-wavelength (ion-scale) ion temperature gradient (ITG) mode [2], trapped electron mode (TEM) [3], kinetic ballooning modes (KBMs) [4], micro-tearing (MT) mode [5–7] and the short-wavelength (electron-scale) electron temperature gradient (ETG) mode [8, 9] are well-known instabilities which

could drive micro-turbulence in fusion plasmas. Due to the kinetic nature of these instabilities, first principle gyrokinetic simulations are usually used to assess the turbulence-driven transport, and simulation results were compared with experiments in transport levels (see [10, 11] and references therein), turbulence amplitudes [10, 12] (and references therein) and more sophisticatedly turbulence cross-phase [13] (and references therein). This validation process [14] is crucial since to achieve the prediction capability of the performance of future fusion devices, we have to demonstrate that first-principle gyrokinetic models, which many predictive codes are

<sup>a</sup> Author to whom any correspondence should be addressed.

based on, can reproduce results from current fusion devices. Validation is also a two-way process, meaning that predictions from gyrokinetic simulations constantly inspire new experiments. Such a positive feedback between experiments and simulations is essential to improve theories and numerical codes so that predictive capabilities can be eventually achieved. Furthermore, the validation process can also inform us the regime of validity of present models, i.e. the parameter regime where the models can provide trust-worthy answers, which gives us confidence in using the models and clues to improve the models in different parametric regimes.

Local flux-tube-based gyrokinetic codes have long been used to simulate turbulence transport in tokamaks with successes and discrepancies (see [15] and references therein), essential for the development of local reduced models crucial for the prediction for the performance of future fusion devices [16, 17]. While flux-tube gyrokinetic simulations have been applied to national spherical torus experiment (NSTX) plasmas [11, 18] with mixed results in comparison with experiments, it is well-known that the large  $\rho^*$  in spherical tokamaks (note that  $\rho^* \sim 0.01$  for NSTX plasmas), about an order of magnitude larger than that in conventional tokamaks, poses a serious challenge to the flux-tube assumption that  $\rho^*$  approaches zero. However, a serious effort of validating a global gyrokinetic code against real spherical tokamak plasmas is very much lacking even with some recent progress [19, 20].

Here in this paper, we present a validation exercise conducted for the global  $\delta f$  particle-in-cell gyrokinetic tokamak simulation (GTS) code [21] using real spherical tokamak plasma equilibria from NSTX [22]. The GTS code is a global gyrokinetic code with robust capability to simulate turbulence and transport for tokamak experiments. GTS simulations were carried out for both NSTX radio frequency (RF)-heated L-mode and neutral beam injection (NBI)-heated H-mode plasmas, and the predicted turbulence thermal fluxes were compared with experimental values from power balance analysis using the TRANSP code [23]. The TRANSP code is a time dependent tokamak transport and data analysis code which, in its analysis mode, models the evolution of the tokamak plasma based on experimentally measured equilibrium profiles, computing solutions to equations on poloidal field diffusion, particle balance, momentum balance and power balance. Since TRANSP uses experimentally measured profiles, errors from these measurements would certainly be passed on to the final results. We note that the uncertainty in the experimental heat fluxes is mainly due to uncertainties in ohmic heating and measured kinetic profiles. What we found from this validation exercise is that GTS simulations are not able to explain observed electron thermal transport variation in a set of NSTX RF-heated L-mode plasmas before and after a RF-heating cessation, while GTS simulations of the NBI-heated H-mode plasma show decent agreements in ion thermal transport with the experiment. The results from these numerical simulations together with electron-scale turbulence measurements [24] indicate that gradient-driven assumption

(that transport coefficients are assumed to be functions of local mean thermodynamic quantities and their gradients) used in GTS simulations may not be valid in the reported RF-heated L-mode plasmas. While further investigations are required to fully understand this issue, this understanding will help us more confidently predict the confinement performance of ITER and other future magnetic confinement devices.

## 2. Gyrokinetic tokamak simulation (GTS) code

Since the main goal of this paper is to present a validation study of the GTS code using NSTX plasmas, here we provide a more detailed description of the GTS code. The GTS code is a global  $\delta f$  Particle-In-Cell code which solves modern gyrokinetic equation in the conservative form from [19]:

$$\frac{\partial f_a}{\partial t} + \frac{1}{B^*} \nabla_Z \cdot (\dot{Z} B^* f_a) = \sum_b C[f_a, f_b] \quad (1)$$

where  $f_a$  is the particle gyro-center distribution function of species  $a$ ,  $\vec{Z}$  denotes the 5D gyro-center phase space variables,  $\dot{Z}$  describes the drift orbit of the gyro-center in phase space,  $B^* = B + (m_a v_{||} / e_a) \vec{b} \cdot \nabla \times \vec{b}$  with  $v_{||}$ ,  $e_a$  and  $m_a$  as the parallel velocity, particle charge and mass, respectively, and  $C[f_a, f_b]$  is the Coulomb collision operator. The GTS code has a newly improved weight scheme ensuing phase space incompressibility and has full tokamak geometry and global simulation domain (without the local ballooning approximation used in local flux-tube gyrokinetic simulations). The GTS code also has fully kinetic electrons with both trapped and passing electron dynamics. The collision operator used in the GTS code is linearized Fokker-Plank operator with particle, momentum and energy conservation for both electron-electron and ion-ion collisions, and Lorentz operator is used for electron-ion collisions. The GTS code also includes neoclassical physics self-consistently in turbulence simulations (due to the large separation between turbulence time-scale and collision time-scale, neoclassical transport fluxes are not calculated in the GTS code). In this study, only the electrostatic capability of the GTS code is used (its implication on the results presented here will be discussed later in the paper), and the electromagnetic capability is being implemented in the GTS code based on an improved electromagnetic scheme [25]. We note that only using the electrostatic capability of the GTS code is one way to explore the minimum physics for explaining observed thermal transport in the experiments. As we will show later in the paper, the electromagnetic capability is not needed to explain ion thermal transport the NBI-heated H-mode plasma. On the other hand, while we are mostly interested in the core region of the plasmas in this paper, we inevitably will come into the vicinity of the plasma edge in some of our global simulations. The tokamak plasma edge region is characterized as fully nonlinear and electromagnetic [26], and thus an electromagnetic treatment is required. The electromagnetic capability of the GTS code will be used to address this issue in the future.

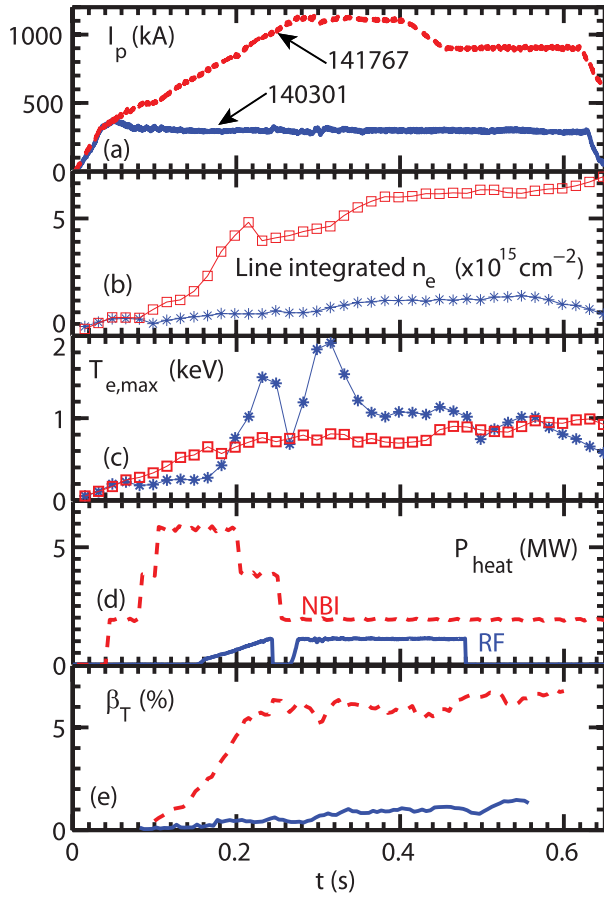


**Figure 1.** The time traces of plasma current,  $I_p$ , (a), line-integrated electron density (b), maximum electron temperature,  $T_{e,max}$ , (c), injected auxiliary heating power,  $P_{heat}$ , (d) and total toroidal beta,  $\beta_T$ , for shots 140301 (blue) and 141767 (red). Different symbols are also used in (b) and (c): asterisks (140301) and open squares (141767). Solid and dashed lines are used for 140301 and 141767, respectively, in other panels.  $P_{heat}$  for shot 140301 denotes the injected RF heating power and for shot 141767,  $P_{heat}$  denotes the injected NBI power.

### 3. Simulation results

In order to explore the regime of validity of the GTS code, it was applied to two quite different NSTX plasmas: one is a RF-heated L-mode plasma (shot 140301) with  $B_T = 5.5$  kG and  $I_p = 300$  kA and the other is a NBI-heated H-mode plasma (shot 141767) with  $B_T = 5.5$  kG and  $I_p$  of about 1 MA. Here, we would like to point out that the RF heating on NSTX uses high harmonic fast wave (HHFW) [27]. The HHFW provides core electron heating and the power deposition peaks in the center of the plasma. We note that both plasmas show strong changes in electrons-scale turbulence (measured by a high-k scattering system [28]) due to a controlled change in either auxiliary heating (shot 140301) or plasma current (shot 141767) (see [24, 29] for more details). Particularly, for shot 140301, the change in the electron-scale turbulence was observed to correlate with the RF cessation occurring at about  $t = 479.6$  ms (see figure 1(d)), and for shot 141767, the change in the electron-scale turbulence was observed to be

caused by a controlled  $I_p$  ramp-down from about 1.1 MA at  $t = 400$  ms to about 0.9 MA at  $t = 460$  ms (see figure 1(a)). For each plasma, GTS simulations were carried out using experimental equilibria both before and after the controlled changes, i.e. before ( $t = 465$  ms) and after ( $t = 482$  ms) the RF cessation for shot 140301, and before ( $t = 332$  ms) and after ( $t = 565$  ms) the current ramp-down for shot 141767. Since carrying out multi-scale global nonlinear simulations is prohibitively expensive with the present-day computational power, here we chose to focus on ion-scale simulation only. To provide some further comparisons between the two shots, we also note that while shot 140301 has higher or comparable maximum  $T_e$ ,  $T_{e,max}$ , compared with shot 141767 (figure 1(c)), shot 141767 has much higher line-integrated density (thus also higher  $\beta_T$ ) than shot 141302 (figures 1(b) and (e)). This higher  $\beta_T$  of shot 141767 may have implications for electron thermal transport which will be discussed later in the paper. Figure 1(c) also shows that the RF cessation at  $t = 479.6$  ms does lead a minor reduction (about 6%) of the reduction in  $T_{e,max}$  from  $t = 465$  ms to 482 ms (note that  $t = 482$  ms is only about 2 ms after the RF cessation), and a bigger reduction in  $T_{e,max}$  (about 27%) is seen from  $t = 482$  ms to 498 ms, about 18 ms after the RF cessation (note that these time points are exact Thomson scattering measurement time points).

#### 3.1. Results for the RF-heated L-mode plasma

Here we first present results from GTS simulations of shot 140301. Using global GTS simulations for this shot was motivated by the fact that local linear and nonlinear gyrokinetic simulations failed to explain observed fast response of electron-scale turbulence to auxiliary heating cessation and reduction in electron heat flux after the RF cessation in shot 140301 and other similar discharges [24, 30] due to measured small changes in local equilibrium quantities in the turbulence measurement region before and after the RF cessation. Particularly, it was found in these RF-heated L-mode plasmas that, following the cessation of RF heating occurring in less than 200  $\mu$ s, a reduction in electron-scale turbulence spectral power was observed to occur on a short time scale of 0.5–1 ms, much smaller than the energy confinement time of about 10 ms, and a factor of 2 decrease in electron heat flux was inferred from power balance analysis after the cessation of RF heating. Global simulations, including profile variation effects (e.g. turbulence spreading [31]), might help to explain the experimental observations.

The choice of radial simulation domain for GTS simulations is facilitated by local linear gyrokinetic stability analyses using the GS2 gyrokinetic code [32]. The GS2 code is an initial value gyrokinetic code which, in its linear mode, finds the fastest growing mode for a given pair of poloidal and radial wavenumbers. We note the collision effects are included in all linear GS2 simulations with Lorentz operator (pitch-angle scattering). Figure 2(a) shows the GS2-calculated ion-scale maximum linear growth rate,  $\gamma_{max}$ , real frequency at maximum linear growth rate,  $\omega_{\gamma_{max}}$ , and the  $E \times B$  shearing rate [33],  $\gamma_{E \times B}$ , at several radial locations for  $t = 482$  ms (after the

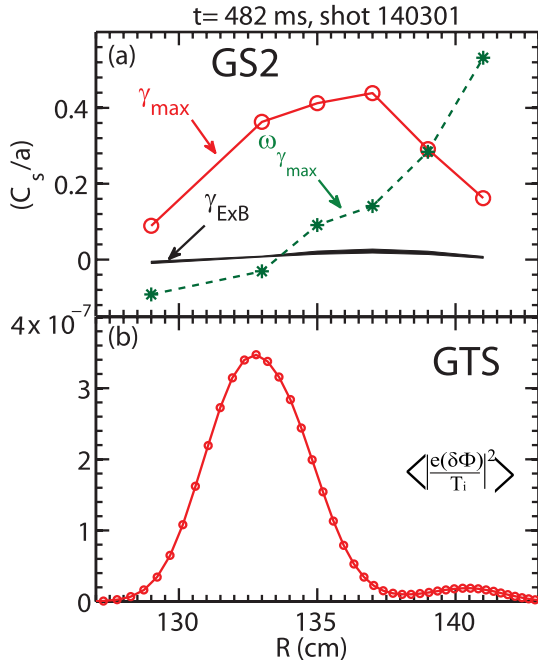


**Figure 2.** (a) Radial profiles of ion-scale maximum linear growth rate,  $\gamma_{\max}$ , (red open circle), real frequency at maximum linear growth rate,  $\omega_{\gamma_{\max}}$ , (green asterisks) and the  $E \times B$  shearing rate,  $\gamma_{E \times B}$ , (black band) for  $t = 482$  ms. Note that the vertical width of the black band denotes experimental uncertainties of  $\gamma_{E \times B}$ . (b) The normalized flux-surface-averaged fluctuations intensity,  $\langle |e(\delta\phi)/T_i|^2 \rangle$ , profile during the linear phase of the GTS simulation.

RF cessation). We note that with the TRANSP code, the ExB shearing rate shown in figure 2(a) is calculated using radial electric field obtained from impurity radial force balance using measured impurity toroidal rotation, measured impurity pressure and calculated neoclassical poloidal flow. The impurity toroidal rotation and pressure are both measured by the charge exchange recombination spectroscopy (CHERS) diagnostic [34] with neutral beam blips (one blip from  $T = 430$  to 445 ms and the second blip from  $t = 490$  to 555 ms). We emphasize that the ExB shear shown here (as the ExB shear used in the simulations in the rest of the paper) is only the mean shear, lacking the self-consistent features that would exist in a flux-driven simulation, e.g. corrugation. It is clear that  $\gamma_{\max}$  peaks around  $R = 135$  cm and drops substantially towards both the plasma core and edge. The real frequency of the most unstable mode goes from negative (electron diamagnetic drift direction) at  $R \approx 130$  cm to positive (ion diamagnetic drift direction) at  $R \approx 140$  cm, showing that there may be a transition from the TEM-like mode to the ITG-like mode from the plasma core to the edge. Further local linear stability analysis (not shown) at  $R = 135$  by scanning the normalized electron temperature gradient,  $a/L_{T_e}$ , and the normalized ion temperature gradient,  $a/L_{T_i}$ , (with  $\beta'$  fixed) shows that the ion-scale modes are actually driven unstable by both electron and ion temperature gradients ( $a$  is the half width of the last closed flux surface;  $L_{T_e}$  and  $L_{T_i}$  are the electron and ion temperature gradient scale lengths, respectively;  $\beta$  is the local plasma

beta). The  $\gamma_{E \times B}$  can be seen to be close to zero, consistent with a small toroidal rotation observed in these RF-heated plasmas, and is much smaller than the  $\gamma_{\max}$  of the unstable ion-scale modes, which supports our approach of using nonlinear ion-scale simulations. The radial profile of  $\gamma_{\max}$  helped us to choose a radial domain from  $\Psi_N = 0.35$  to 0.7 ( $R \sim 125$  cm to 145 cm) for global nonlinear GTS simulations, where  $\Psi_N$  is the square root of the normalized toroidal flux. We note that an additional buffer region with a width of  $\nabla\Psi_N = 0.1$  is used on each side of the simulation domain (also see figure 3). The size of grids on poloidal planes is about local  $\rho_i$ , and 80 particles per cell-species were used. For comparison, the normalized flux-surface-averaged fluctuation intensity,  $\langle |e(\delta\phi)/T_i|^2 \rangle$ , profile during the linear phase of the GTS simulation is shown in figure 2(b), where  $\delta\phi$  is the potential fluctuation,  $e$  is the electron charge,  $T_i$  is the ion temperature at the selected reference point of  $\Psi_N = 0.5$  and  $\langle \dots \rangle$  denotes flux-surface average. Note that with  $E \times B$  shear effect included in the simulation, the fastest growing location in the GTS simulation in the linear phase is shifted towards a smaller radius compared with the radial profile of  $\gamma_{\max}$  in figure 2(a). It is also clear that the fluctuation intensity profile in figure 2(b) shows two radially-localized unstable regions, one centered around  $R = 133$  cm and the other centered around  $R = 141$  cm, with higher linear growth rates for the modes in the radial region at the smaller radius. The difference in linear growth rates in the two radially-localized unstable regions is consistent with the local linear stability analysis shown in figure 2(a) which shows larger linear growth rates at  $R = 133$  cm than at  $R = 141$  cm. We also note that the modes in the weakly growing region around  $R = 140$ , although close to the outer buffer region, is not as important as the fastest growing modes in the center of the simulation domain during the nonlinear quasi-steady-state phase (see figure 4).

Since the GTS code is gradient driven, here we show driving equilibrium gradient and  $q$  profiles in the GTS simulation domain (from  $\Psi_N = 0.35$  to 0.7 with a buffer region of the width of  $\nabla\Psi_N = 0.1$  on both sides) in figure 3 for two time points, i.e.  $t = 465$  ms and  $t = 482$  ms, in physical space. We emphasize that the simulation domain of  $\Psi_N = 0.35$  to 0.7 shown in figure 3 is far from the plasma edge region which a  $\delta f$  gyrokinetic code may have difficulty to handle. It is clear from figure 3 that the normalized ion temperature gradient,  $R_0/L_{T_i}$ , (figure 3(a)) and the normalized electron temperature gradient,  $R_0/L_{T_e}$ , (figure 3(b)) ( $R_0$  is the major radius of the magnetic axis) have an overall trend of increasing from the plasma core to the edge, increasing from about 5 near the inner buffer region to about 12.5–17 near the outer buffer region for both time points. Furthermore, for both time points, although  $T_e$  is everywhere higher than  $T_i$  in these RF-heated L-mode plasmas in the simulation domain by about 50% (note that RF in NSTX heats electrons), the two temperature gradients seen in figures 3(a) and (b) are quite similar to each other (less than 25% in difference) for most part of the simulation domain except very close to the outer buffer region, which supports that the unstable ion-scale modes are driven by both



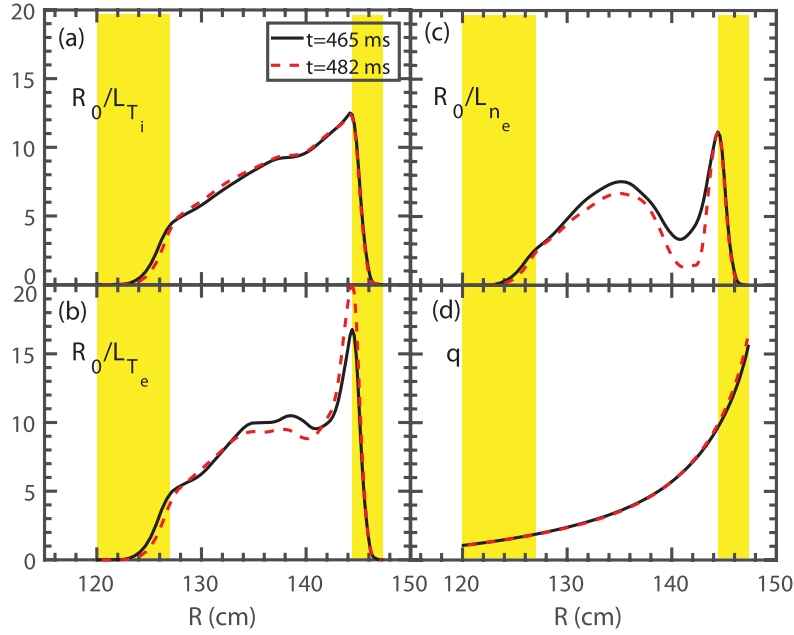


**Figure 3.** (a) Radial profiles of normalized ion temperature gradient,  $R_0/L_{T_i}$ , for  $t = 465$  ms (black solid line) and  $t = 482$  ms (red dashed line) (same legend for the other panels); (b) radial profiles of normalized electron temperature gradient,  $R_0/L_{T_e}$ ; (c) radial profiles of normalized electron density gradient,  $R_0/L_{n_e}$ ; (d) radial profiles of safety factor,  $q$ . The simulation domain is from  $\Psi_N = 0.35$  to  $0.7$  ( $R \approx 127$  cm to about  $145$  cm) for both time points. Note that in addition to the simulation domain, two buffer regions of a width of  $\nabla\Psi_N = 0.1$  are used in the simulation, as denoted by the yellow rectangles in the panels for  $t = 465$  ms as an example.

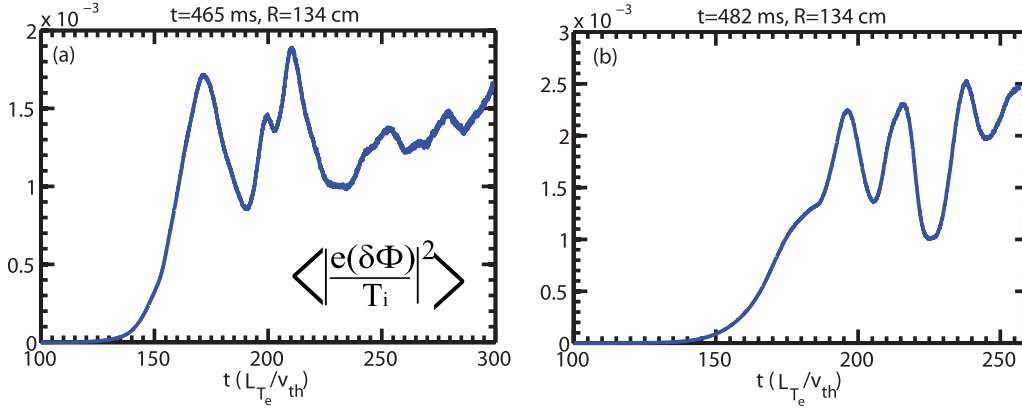


**Figure 4.** The normalized flux-surface-averaged fluctuation intensity,  $\langle |\frac{e\delta\phi}{T_i}|^2 \rangle$ , temporal evolutions at  $R = 134$  cm for  $t = 465$  (a) and  $482$  ms (b). Note that the time is normalized to  $L_{T_e}/V_{th}$ , where  $L_{T_e}$  is the scale length of the electron temperature gradient and  $V_{th}$  is the ion thermal velocity with all physical quantities taken at the reference location of  $\Psi_N = 0.5$ .

temperature gradients. On the other hand, the normalized electron density gradient (figure 3(c)) is everywhere smaller than the two normalized temperature gradient, only close to  $R_0/L_{T_i}$  in a limited radial range around  $R = 133$  cm. The  $q$  profile is monotonic and is about 2 near the inner buffer region and about 10 near the outer buffer region (note that these RF-heated plasmas are of high  $B_T$  of 5.5 kG and low  $I_P$  of 300 kA). Comparing these profiles between the two time points, we can see that while there is only minimum in  $R_0/L_{T_i}$  and  $q$ , the changes in  $R_0/L_{n_e}$  and  $R_0/L_{T_e}$  from  $t = 465$  to  $482$  ms at  $R = 135$  cm (center of the simulation domain) is about 11% and 7%, respectively. We emphasize that these small changes

in driving gradients would predict small changes in resulting thermal transport as shown in figure 6 below.

In order to demonstrate the turbulence growth and saturation in these GTS simulations, temporal evolutions of  $\langle |\frac{e\delta\phi}{T_i}|^2 \rangle$  at  $R = 134$  cm for both the  $t = 465$  and  $482$  ms cases are shown in figures 4(a) and (b), respectively ( $R = 134$  cm is close to the center of the simulation domain). Figure 4 shows that although  $\langle |\frac{e\delta\phi}{T_i}|^2 \rangle$  grows faster in the simulation for the  $t = 465$  ms case than for the  $t = 482$  ms case, but it reaches saturation earlier for the  $t = 465$  ms case. As a result, the saturation levels of  $\langle |\frac{e\delta\phi}{T_i}|^2 \rangle$  at  $R = 134$  cm for both the  $t = 465$  ms

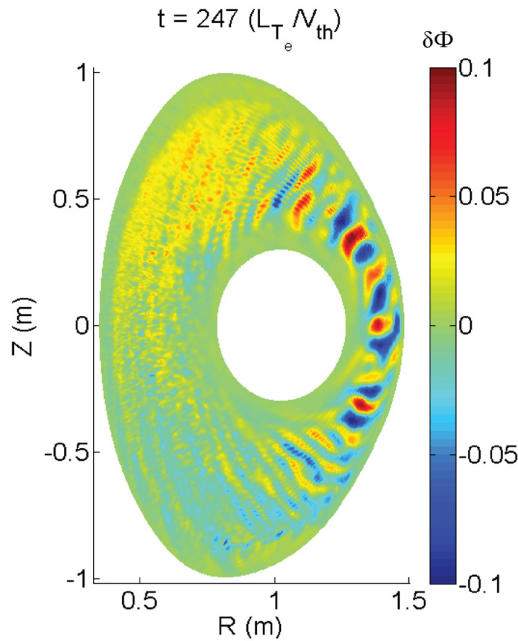


**Figure 5.** The poloidal cross-section of the normalized potential fluctuation,  $\frac{e\delta\phi}{T_e}$ , at  $t = 247 (L_{Te}/V_{th})$  which is well in the saturation phase.

and  $t = 482$  ms cases are similar. Furthermore, both simulations show large oscillations in the saturation phase, which is typical for global gyrokinetic simulations. Nevertheless, we emphasize that in both cases turbulence intensity reaches a quasi-steady-state period after the initial fast growth.

To provide a visual presentation of the nonlinearly saturated ion-scale turbulence, the poloidal cross-section of the normalized potential fluctuation,  $\frac{e\delta\phi}{T_e}$ , is plotted in figure 5 at  $t = 247 (L_{Te}/V_{th})$  which is well in the saturation phase. It can be clearly seen that large turbulence eddies with radially elongated structures are formed during the turbulence saturation phase with radial extensions of about half of the radial simulation domain. These radially elongated eddies are responsible for driving both the electron and ion thermal transports. The observed temporal evolution of the turbulence in the simulation demonstrates that it propagates in the electron diamagnetic direction, which is consistent with the propagation direction of the linearly unstable mode (figure 2(a)) at the fastest growing location seen in the GTS simulation (figure 2(b)). Furthermore, the observed turbulence is the strongest at the outer mid-plane, which is consistent with the well-know ballooning structure of drift turbulence in tokamak toroidal geometry. By analyzing turbulence at one flux surface at  $R = 133$  cm from the nonlinear GTS simulation, it is found that the mode with the highest saturated amplitude has a poloidal wavenumber ( $m$ ) of about 45 and a toroidal wavenumber ( $n$ ) of about 15, corresponding to a  $k_{\theta}\rho_s$  of about 0.2, and in comparison, the most unstable mode in the linear phase at the same radial location has  $m \approx 60$  and  $n \approx 20$ , corresponding to a  $k_{\theta}\rho_s$  of about 0.3. Thus, a downshift in the

wavenumber spectrum in the nonlinearly saturated phase occurs in the simulation. We also note that in the GTS simulations, the experimental equilibrium  $E \times B$  shear is turned on from the beginning (actually the  $E \times B$  shear showed a small but destabilization effect, compared to the simulations without the  $E \times B$  shear).

Here, we present the comparison between experiments and GTS simulations in terms of thermal transports. We note that figure 6(a) has been published in [24] as a part of an effort to understand the observed fast response of electron-scale turbulence to the RF cessation. Since the result shown in figure 6(a) is also an essential part of this paper, we will present the result in the present context as follows. Figure 6(a) compares electron energy flux,  $Q_{e,GTS}$ , radial profiles at  $t = 465$  (with RF heating) and 482 ms (after the RF cessation) from GTS simulations with those of the inferred electron heat flux,  $Q_{e,exp}$ . It can be clearly seen that while  $Q_{e,GTS}$  is essentially the same for both  $t = 465$  ms and  $t = 482$  ms at  $R \gtrsim 136$  cm,  $Q_{e,GTS}$  at  $R \lesssim 134$  cm is larger at  $t = 482$  ms than at  $t = 465$  ms. The observed change in  $Q_{e,GTS}$  before and after the RF cessation is opposite to the change in experimental electron heat flux,  $Q_{e,exp}$ , from the power balance analysis, in which  $Q_{e,exp}$  at  $t = 465$  ms is about a factor of 2 higher than  $Q_{e,exp}$  at  $t = 482$  ms. Furthermore,  $Q_{e,GTS}$  at  $t = 465$  and 482 ms both show good agreement with  $Q_{e,exp}$  at  $t = 482$  ms for  $R \lesssim 138$  cm but not with  $Q_{e,exp}$  at  $t = 465$  ms when  $Q_{e,exp}$  is about a factor of 2 higher due to the RF heating. We note that the decrease in  $Q_{e,GTS}$  towards larger radius at  $R > 138$  cm is probably due to interactions with a buffer region from  $R \approx 145$  to 147 cm and this will be investigated in future simulations with an enlarged simulation domain. Predicted ion thermal transport is shown in figure 6(b), where changes in  $Q_{i,GTS}$  between  $t = 465$  and 482 ms is seen to be similar to that of  $Q_{e,GTS}$ . However, the predicted  $Q_{i,GTS}$  is significantly larger than  $Q_{i,exp}$  (which is essentially the same before and after the RF cessation) around  $R = 135$  cm, and the reason behind this is still under investigation. Similar as  $Q_{e,GTS}$ ,  $Q_{i,GTS}$  also decreases towards the boundary of the simulation domain and this issue will be addressed in the future together with  $Q_{e,GTS}$  as discussed above. Nevertheless, these GTS simulation results are still consistent with previously-mentioned linear and nonlinear local electromagnetic gyrokinetic simulations (not shown) which showed that the observed equilibrium profile changes cannot explain the reduction in  $Q_{e,exp}$  before and after the RF cessation [24]. The main reason behind this is that the observed equilibrium changes between  $t = 465$  and 482 ms were shown to be less than 15% around  $R = 135$  cm (also see figure 3), and, unless the transport is very stiff or close to instability threshold, gradient-driven simulations (both local and global) should show similar amount of thermal transport at both times. This is exactly what is seen in figure 6. In order to assess the sensitivity of the instability and turbulence on  $T_e$  gradient, we have conducted extensive local linear stability analysis and nonlinear gyrokinetic simulations (using GYRO [35]) as discussed in [24]. Local linear stability shows that both ion and electron-scale modes are robustly unstable in the high- $k$  measurement region, i.e. around  $R = 135$  cm. Local

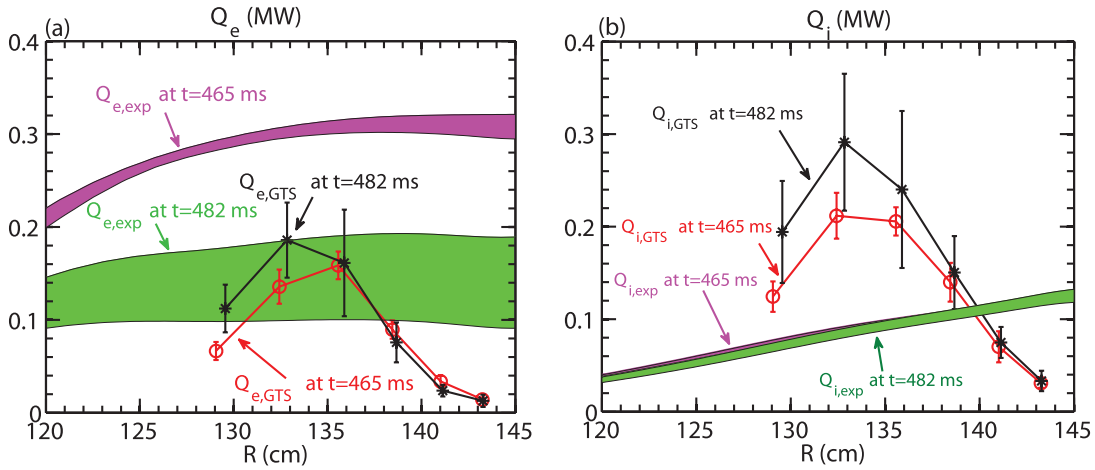


**Figure 6.** (a) Electron thermal transport: red circles: electron energy flux,  $Q_{e,GTS}$ , at  $t = 465$  ms (before the RF cessation) as a function of major radius from nonlinear GTS simulation; black asterisks:  $Q_{e,GTS}$  at  $t = 482$  ms (after the RF cessation) from nonlinear GTS simulation; magenta band: radial profile of experimental electron heat flux,  $Q_{e,exp}$ , at  $t = 465$  ms from power balance analysis; green band: radial profile of  $Q_{e,exp}$  at  $t = 482$  ms. Note that the vertical widths of the magenta and green bands denote the experimental uncertainties.  $Q_{e,GTS}$  is averaged over a quasi-steady saturation period, and the errorbars of  $Q_{e,GTS}$  are the standard deviation of  $Q_{e,GTS}$  in the averaging time period. Reprinted from [24], with the permission of AIP Publishing. (b) Ion thermal transport with the same denotations as in (a).

nonlinear gyrokinetic simulations around the same radial locations show that the ion-scale turbulence can drive significant turbulence fluxes well exceeding the experimental value, and varying  $T_e$  and  $T_i$  gradients by  $\pm 25\%$  did not significantly change turbulence fluxes, meaning that the stiffness in  $T_e$  and  $T_i$  profiles is rather weak. On the other hand, electron thermal transport from local nonlinear ETG simulations significantly under-predicted experiments. Furthermore, we would like to point out that ideally for our purpose, we would need to compare  $T_e$  profiles right before and after the RF cessation for the RF-heated L-mode case. However, the small variation ( $\sim 3.6\%$ ) in  $T_e$  in the high- $k$  measurement region (around  $R = 135$  cm) from  $t = 465$  ms to 482 ms over 16 ms indicates that  $T_e$  is quite stationary before the RF cessation and that the changes in  $T_e$  in the high- $k$  measurement region right before and after the RF cessation is much smaller than 3.6% seen from  $t = 465$  ms to 482 ms. Thus, based on the results above, we conclude that the observed profile changes in the simulation domain are not likely able to explain the observed reduction in electron thermal transport. However, we note that our conclusion only results from local and global gradient-driven  $\delta f$  simulations using codes including GS2, GYRO and GTS. To fully address the observation in this RF-heated L-mode plasma, the change in heating due to the RF cessation has to be taken into account, and thus flux-driven full  $f$  simulations [36–39], which allow mean profiles to vary and include sources and sinks, have to be used, which is beyond the scope of the paper and can only be addressed in future work.

In addition to the global effects which are partly addressed by using the GTS code as presented above, there are other possible physical mechanisms that we would like to discuss. One is the recent finding of the physics near marginality [40–42], where gradient-driven simulations were shown to have difficulty to handle turbulent dynamics close the nonlinear turbulence threshold, e.g. turbulence spreading,

avalanches, self-organized flow structure and its shear (i.e. the  $E \times B$  staircase) [36, 37, 43–46]. Particularly, it was shown that the  $E \times B$  staircase structure is smeared out in gradient-driven simulations with comparable ambient gradient drives as flux-driven simulations [46]. We note that these flux-driven phenomena are important for producing multi-valued flux-gradient relations which are required to explain our experimental observation, i.e. fast change in electron-scale turbulence and electron thermal transport without significant change in equilibrium profiles [24]. Although, as we presented above, our linear and nonlinear simulations have demonstrated that the ion-scale and electrons-scale modes are robustly unstable in this RF-heated L-mode plasma and they are likely not near marginal state, to fully explore the issue of marginality flux-driven full  $f$  simulations [36–39] with appropriate boundary conditions [47] have to be applied and can only be subjected to future exploration. Furthermore, the mechanism of multiscale interaction between ion and electron-scale turbulence [48, 49] may play a role, and from what we have studied, we cannot fully rule out this possibility which is subject to future study with local flux-tube simulations using gyrokinetic codes, such as GYRO.

### 3.2. Results for the NBI-heated H-mode plasma

Having shown the gradient-driven GTS simulations were not able to account for the observed electron thermal transport variation associated with the RF cessation in some RF-heated L-mode plasmas, here we show that good agreement can be achieved in ion thermal transport between ion-scale GTS simulations and experiment for an NSTX NBI-heated H-mode plasma (shot 141767), where electron-scale turbulence was observed to be reduced/stabilized by an increase in the electron density gradient induced by the controlled Ip ramp-down shown in figure 1(a) [29]. We focus on ion-scale simulation



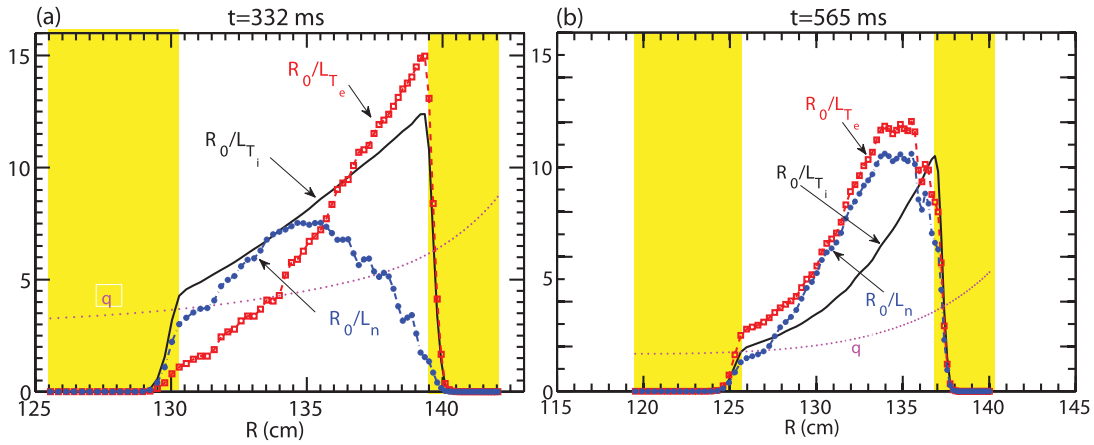


**Figure 7.** (a) Radial profiles of normalized equilibrium gradients and safety factor at  $t = 332$  ms: normalized electron temperature gradient,  $R_0/L_{T_e}$  (red open square), normalized electron density gradient,  $R_0/L_n$  (blue asterisks), normalized ion temperature gradient,  $R_0/L_{T_i}$  (black solid line) and safety factor,  $q$  (magenta dashed line). The simulation domain is from  $\Psi_N = 0.55$  to  $0.8$  ( $R \approx 130$  cm to about  $139.5$  cm). (b) The same as (a) but for  $t = 565$  ms, except that the simulation domain is from  $\Psi_N = 0.35$  to  $0.8$  ( $R \approx 125.5$  cm to about  $137$  cm). The yellow rectangles in (a) and (b) denote the buffer regions in the simulation and each has a width of  $\nabla\Psi_N = 0.1$ , not counted as part of the simulation domain.

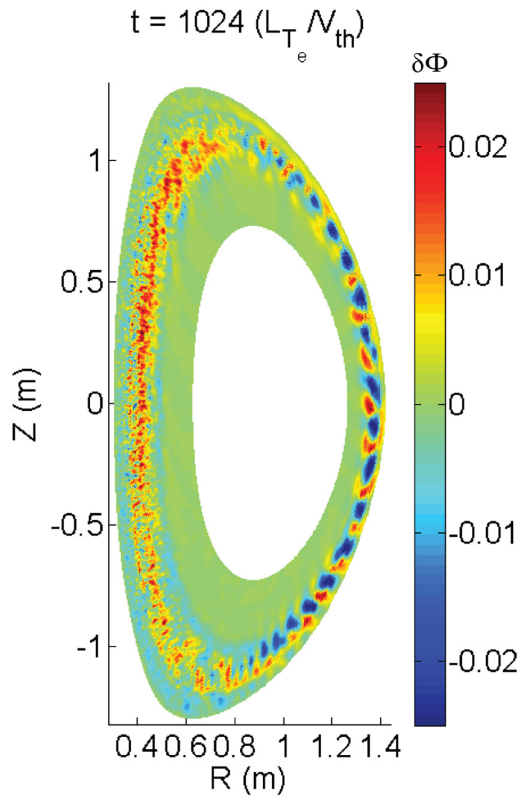
and apply the GTS code to two time points, i.e. before and after the  $I_p$  ramp-down as discussed previously. For these simulations, 40 particles per cell-species were used with the size of grids on poloidal planes is about local  $\rho_i$ . Figures 7(a) and (b) show the simulation domains together with the radial profiles of some normalized equilibrium gradients and the safety factor,  $q$ , for  $t = 332$  ms and  $565$  ms, respectively. The simulation domains were chosen to cover a radial region with large core equilibrium gradients but to avoid the pedestal region with which a  $\delta f$  code like GTS may have difficulty. It is clear that the normalized density gradient at  $R = 135$  cm becomes much larger at  $t = 565$  ms than  $t = 332$  ms, consistent with the density profile steepening following the  $I_p$  ramp-down, while the normalized ion temperature gradient become smaller at  $t = 565$  ms. We also note that since the current did not fully relax during the discharge, core  $q$  values continue to decrease. We would like to point out that the significant increase in the density gradient after the current ramp-down would have a stabilization effect on ITG modes. However, it is found that the unstable ion-scale modes are of an ITG/TEM hybrid which actually can be driven more unstable by the large density gradient.

The poloidal cross-section of  $\frac{e\delta\phi}{T_i}$  is plotted in figure 8 at  $t = 1024$  ( $L_{T_e}/V_{th}$ ) (well in the saturation phase) from the GTS simulation using the plasma equilibrium at  $t = 332$  ms (figure 7(a)). It is evident that this H-mode plasma is much more strongly shaped than the L-mode plasma shown in figure 5. It can be clearly seen that large turbulence eddies are formed during the turbulence saturation phase with radial extensions across the whole outer half of the radial simulation domain. These large-scale eddies are responsible for driving the observed ion thermal transport. The temporal evolution of these eddies seen in the simulation shows that they propagate in the ion diamagnetic direction, which is due to the large Doppler shift toward ion direction resulting from the large toroidal flow driven by the NBI heating. Similar to figure 5,

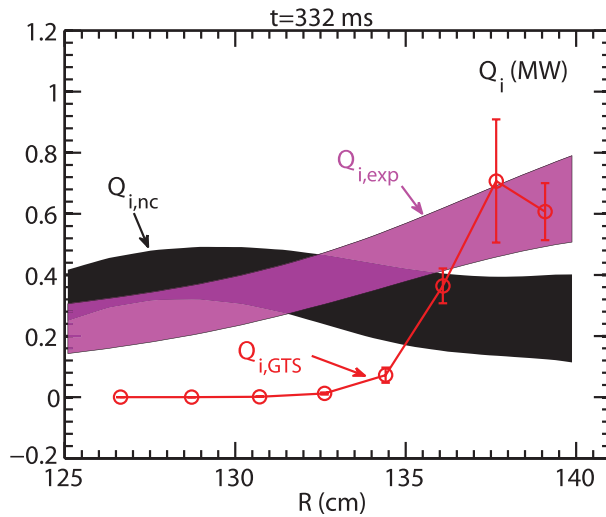
a clear ballooning structure in the poloidal distribution of the turbulence eddies can be seen in figure 8. Analyses of turbulence mode numbers at the flux surface at  $R = 137.5$  cm show a poloidal wavenumber ( $m$ ) of about 120 and a toroidal wavenumber ( $n$ ) of about 23, corresponding to a  $k_{\theta}\rho_s$  of about 0.2, for both linear and nonlinear phases, demonstrating that the most unstable modes in the linear phase eventually becomes the modes with the highest saturated amplitude in the nonlinear phase, not showing the spectral downshift seen in the simulation for shot 140301. Similar to the GTS simulations presented in the section above, the experimental equilibrium  $E \times B$  shear is turned on from the beginning of the simulation.

Figure 9 compares the simulated ion energy flux,  $Q_{i,GTS}$ , radial profiles at  $t = 332$  from the GTS simulation with those inferred from the experiment, along with neoclassical ion heat flux,  $Q_{i,nc}$ , from NCLASS [50]. It can be seen that  $Q_{i,exp}$  is comparable to  $Q_{i,nc}$  at  $R \lesssim 132$  cm, which is consistent with the very small  $Q_{i,GTS}$  there. At larger radius, i.e.  $R \gtrsim 136$  cm,  $Q_{i,GTS}$  is significantly larger than those at smaller radius, consistent with  $Q_{i,exp}$  being significantly larger than  $Q_{i,nc}$ . In fact, taken into account the errorbars and uncertainties in  $Q_{i,GTS}$ ,  $Q_{i,exp}$  and  $Q_{i,nc}$ ,  $Q_{i,GTS} + Q_{i,nc}$  is approximately equal to  $Q_{i,exp}$ , indicating that the ion-scale turbulence is responsible for the observed anomalous ion thermal transport at this time point of the discharge.

Having presented the results from the GTS simulation for  $t = 332$  ms of the H-mode plasma, here we present the simulation results for  $t = 565$  ms. Figure 10 plots the same quantities as in figure 9 but for  $t = 565$  ms. We emphasize that the GTS simulation for  $t = 565$  ms does not predict any meaningful ion heat flux throughout the whole simulation domain (so  $Q_{i,GTS}$  is plotted as zero in figure 10). However, this is still in agreement with the experiment, as  $Q_{i,exp}$  is approximately equal to  $Q_{i,nc}$ , and turbulence-driven ion thermal transport is therefore not needed. Thus, we conclude, from both figures 9 and 10, that the GTS simulation results are in reasonable agreement



**Figure 8.** The poloidal cross-section of the normalized potential fluctuation,  $\frac{e\delta\phi}{T_e}$ , at  $t = 1024 (L_{T_e}/V_{th})$  which is well in the saturation phase.



**Figure 9.** Red circles: ion energy flux,  $Q_{i,GTS}$ , as a function of major radius from a nonlinear GTS simulation of shot 141767 at  $t = 332$  ms; magenta band: radial profile of experimental ion heat flux,  $Q_{i,exp}$ , at  $t = 332$  ms from power balance analysis; black band: radial profile of neoclassical ion heat flux,  $Q_{i,nc}$ . The same definition of uncertainties and errorbars applies as in figure 6.

in ion thermal transport with this and other similar H-mode plasmas. However, from the GTS simulation for  $t = 565$  ms shown in figure 10 alone, we cannot see the reason for the total

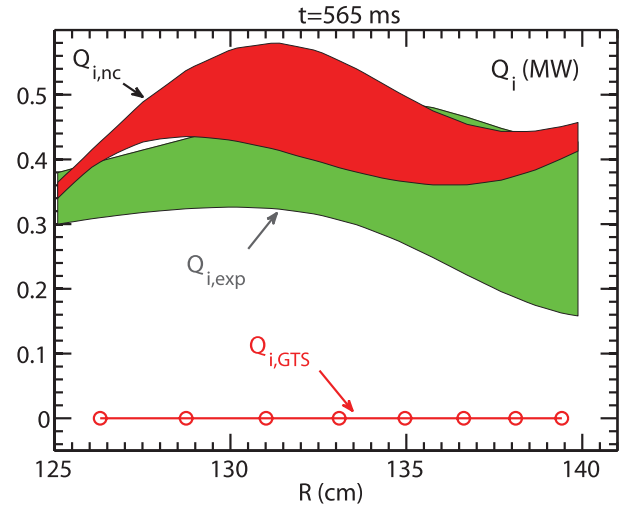


**Figure 10.** Red circles: ion energy flux,  $Q_{i,GTS}$ , as a function of major radius of a nonlinear GTS simulation of the same shot but at a different time point of  $t = 565$  ms; green band: radial profile of experimental ion heat flux,  $Q_{i,exp}$ , at  $t = 565$  ms from power balance analysis; red band: radial profile of neoclassical ion heat flux,  $Q_{i,nc}$ . The same definition of uncertainties and errorbars applies as in figure 6.

suppression of ion-scale turbulence in the simulation. We note that for the GTS simulations shown in both figures 9 and 10, the  $E \times B$  shear is turned on from the beginning of the simulations. In order to assess the effects of the  $E \times B$  shear, a GTS simulation without the  $E \times B$  shear for  $t = 565$  ms was carried out. Figure 11 shows that without the  $E \times B$  shear,  $\langle |\frac{e\delta\phi}{T_e}|^2 \rangle$  grows nicely and reaches quasi-steady nonlinearly saturated state. However, as shown in figure 11, another GTS simulation with the  $E \times B$  shear turned on during the simulation demonstrates that the turbulence is almost immediately suppressed and remains at negligible levels for the remaining of the simulation. Thus, the  $E \times B$  shear is responsible for the neoclassical level of ion thermal transport at  $t = 565$  ms, consistent with previous observations [51]. The total suppression of ion-scale turbulence for the H-mode case at  $t = 565$  ms by the ExB shear was a surprise, since linear GS2 simulations (not shown) around the region of significant density gradient increase actually showed that ion-scale modes at  $t = 565$  ms are as unstable as, if not even more than, those at  $t = 332$  ms (we note that the linear GS2 simulations do not have ExB shear effects included). On the other hand, the neoclassical level of ion thermal transport, due to the suppression of ion-scale turbulence by the ExB shear, is the hallmark of NSTX H-mode plasmas [51]. We note that due to the small aspect ratio, spherical tokamaks with tangential neutral beam injection heating typically have strong toroidal flow with Mach number approaching 1, leading to a large enough ExB shearing rate to suppress ion-scale turbulence.

In addition to driving ion thermal transport as shown in figure 9, the ion-scale turbulence in the GTS simulation for  $t = 332$  ms can also drive electron thermal transport, and its comparison with the experiment is shown in figure 12. It is clear that the predicted electron thermal transport,  $Q_{e,GTS}$ , is

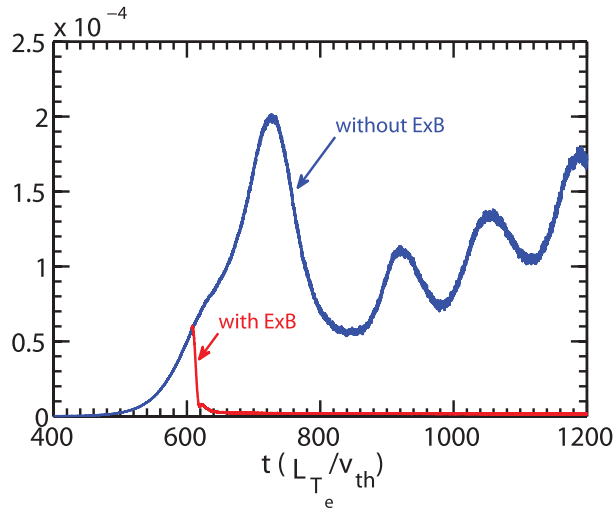


**Figure 11.** The temporal evolution of the normalized flux-surface-averaged fluctuation intensity,  $\langle |\frac{e\delta\phi}{T_e}|^2 \rangle$ , at  $R \approx 135$  from GTS simulations for  $t = 565$  ms without  $E \times B$  shear (solid blue line) and with  $E \times B$  shear turned on during the simulation (red solid line).

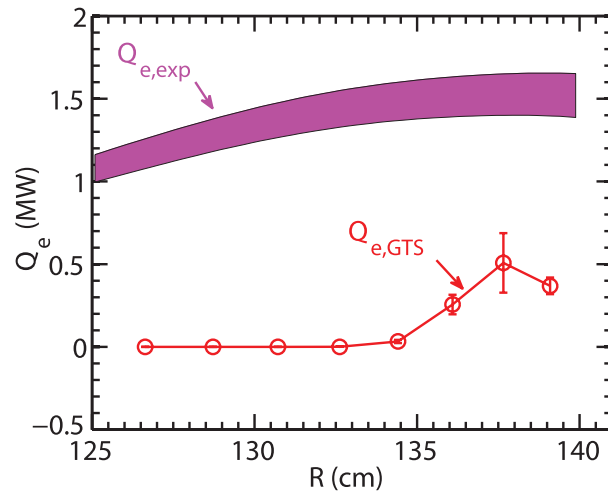


**Figure 12.** Red circles: electron energy flux,  $Q_{e,GTS}$ , as a function of major radius from a nonlinear GTS simulation of shot 141767 at  $t = 332$  ms; magenta band: radial profile of experimental electron heat flux,  $Q_{e,exp}$ , at  $t = 332$  ms from power balance analysis. The same definition of uncertainties and errorbars as in figure 6 also applies here.

much smaller than the experimental value,  $Q_{e,exp}$ . Furthermore, at  $t = 565$  ms, since all ion scale turbulence is suppressed in the GTS simulation, the predicted electron thermal transport is zero as  $Q_{i,GTS}$  shown in figure 10. We note that this shortfall in  $Q_{e,GTS}$  compared with experimental values is not surprising since these ion-scale GTS simulations do not capture the residual ETG turbulence that may exist in the plasma. We also note that although linear GS2 simulations have shown that ETG modes are more stable towards the plasma core, ETG modes are found to be unstable around  $R \sim 130$  cm where, seen in figure 12, ion-scale-turbulence-generated electron

energy flux is already negligible. Furthermore, only the electrostatic capability of the GTS code is used in this validation exercise and the electromagnetic effects may well contribute to electron thermal transport. As shown in figure 1(e), shot 141767 has much higher  $\beta_T$  than shot 140301, and thus it is reasonable that electromagnetic effects may be more important for shot 141767 than for shot 140301.

#### 4. Summary and discussion

In summary, global electrostatic GTS simulations have been applied to two quite different NSTX plasmas, one NSTX RF-heated L-mode plasma and one NBI-heated H-mode plasma. In both plasmas, substantial turbulence variation was observed in correlation with controlled variations in experimental conditions, i.e. the RF heating cessation for the L-mode plasma and the  $I_p$  ramp-down for the H-mode plasma [24, 29]. Ion-scale GTS simulations before and after the changes in the experimental conditions for both plasmas were carried out in order to assess the simulation predictions in thermal transport against experimental values from transport analyses using the TRANSP code [23]. It was found that for the L-mode plasma, while the GTS predicted electron thermal transport is in agreement with the experiment after the RF cessation, the GTS-predicted electron thermal transport before the RF cessation is about a factor of 2 smaller than the experimental level. Since the GTS code is gradient-driven and the measured equilibrium profile changes before and after the RF cessation are small, this discrepancy is not surprising. Although profile stiffness may explain the discrepancy between the experiment and simulations at first glance, local linear and nonlinear gyrokinetic simulations have shown that both ion and electron-scale modes are robustly unstable and the resulting turbulence is far from linear and nonlinear threshold [24]. Thus we conclude that the observed profile changes in the simulation domain are not likely able to explain the observed reduction in electron thermal transport before and after the RF cessation in these RF-heated L-mode plasmas. However, such a conclusion only applies to gradient-driven turbulence. To fully explore the physics near marginality [40–42], full  $f$  simulations [36–39] with appropriate boundary condition [47], which allow mean profiles to vary and include flux-drive (e.g. sources and sinks), have to be used and may be able to explain the experiment with properly resolved turbulent dynamics close the nonlinear turbulence threshold, e.g. turbulence spreading, avalanches, self-organized flow structure and its shear (i.e. the  $E \times B$  staircase) [36, 37, 43–46]. Furthermore, multiscale physics with the interaction between ion and electron-scale turbulence [48, 49] may also play a role, which is presently unexplored and is beyond the scope of this paper. These speculations are subjected to future studies.




On the other hand, the GTS simulations applied to the NBI-heated H-mode plasma reproduced quite nicely the observed change in ion thermal transport. Before the current ramp-down in the H-mode plasma, the GTS-predicted ion thermal transport,  $Q_{i,GTS}$ , plus the neoclassical ion thermal transport,

$Q_{i,nc}$ , can explain the experimental ion thermal transport. After the current ramp-down, the experimental ion thermal transport is approximately equal to the calculated neoclassical value, which is again consistent with the corresponding GTS simulation which predicts negligible amount of ion thermal transport generated by turbulence. Furthermore, local non-linear ion-scale gyrokinetic simulations significantly over-predicted experimental value [24]. These results demonstrate that the ion thermal transport can be well explained in the framework of electrostatic turbulence and that global simulation is a requirement. However, in the NBI-heated H-mode plasma, the experimental electron thermal transport could not be explained by the ion-scale GTS simulations, which is also not surprising since these GTS simulations did not have electron-scale resolution to capture the possible residual ETG turbulence in the plasma, which could be important in some regions in the plasma, and no electromagnetic effects are included in the present simulations. Possibly, multi-scale interaction between ion-scale and electron-scale turbulence [48, 49] may also play a role in driving electron thermal transport. In short, the gradient-driven assumption of the GTS code is shown to work better in NBI-heated H-mode plasmas than in certain RF-heated L-mode plasmas. However, despite the progress in the investigation of this issue reported in this paper, the definite reason behind this difference is still not fully understood. Future experiments on the recently commissioned NSTX-U [52] will help us to quantify the regime of validity of gradient-driven GTS simulations.

## Acknowledgment

The authors would like to thank the NSTX team for the excellent technical support for this work. This manuscript is based upon work supported by the U.S. Department of Energy, Office of Science, Office of Fusion Energy Sciences, and has been authored by Princeton University under Contract No. DE-AC02-09CH11466 with the U.S. Department of Energy. This work was also supported by the U.S. Department of Energy under Contracts No. DE-AC02-76CH03073, No. DE-FG03-95ER54295, and No. DE-FG03-99ER54518. The computational resource for the GTS simulations was provided by the National Energy Research Scientific Computing Center.

## ORCID iDs

Y. Ren  <https://orcid.org/0000-0003-4571-9046>  
 W. Guttenfelder  <https://orcid.org/0000-0001-8181-058X>  
 J. Ruiz-Ruiz  <https://orcid.org/0000-0003-4258-5273>

## References

- [1] Tang W. 1978 *Nucl. Fusion* **18** 1089
- [2] Coppi B. and Pegoraro F. 1977 *Nucl. Fusion* **17** 969
- [3] Kadomtsev B. and Pogutse O. 1971 *Nucl. Fusion* **11** 67
- [4] Tang W. et al 1980 *Nucl. Fusion* **20** 1439
- [5] Hazeltine R.D. and Strauss H.R. 1976 *Phys. Rev. Lett.* **37** 102
- [6] Drake J.F. et al 1980 *Phys. Rev. Lett.* **44** 994
- [7] Guttenfelder W. et al 2011 *Phys. Rev. Lett.* **106** 155004
- [8] Lee Y.C. et al 1987 *Phys. Fluids* **30** 1331
- [9] Dorland W. et al 2000 *Phys. Rev. Lett.* **85** 5579
- [10] Holland C. et al 2011 *Phys. Plasmas* **18** 056113
- [11] Ren Y. et al 2012 *Phys. Plasmas* **19** 056125
- [12] Lin L. et al 2009 *Phys. Plasmas* **16** 012502
- [13] White A.E. et al 2010 *Phys. Plasmas* **17** 056103
- [14] Terry P.W. et al 2008 *Phys. Plasmas* **15** 062503
- [15] Garbet X. et al 2010 *Nucl. Fusion* **50** 043002
- [16] Kinsey J.E. et al 2008 *Phys. Plasmas* **15** 055908
- [17] Citrin J. et al 2017 *Plasma Phys. Control. Fusion* **59** 124005
- [18] Ren Y. et al 2013 *Nucl. Fusion* **53** 083007
- [19] Wang W. et al 2015 *Nucl. Fusion* **55** 122001
- [20] Wang W.X. et al 2015 *Phys. Plasmas* **22** 102509
- [21] Wang W.X. et al 2010 *Phys. Plasmas* **17** 072511
- [22] Ono M. et al 2000 *Nucl. Fusion* **40** 557
- [23] Hawryluk R.J. 1981 *Physics of Plasma Close to Thermonuclear Conditions* (New York: Pergamon)
- [24] Ren Y. et al 2015 *Phys. Plasmas* **22** 110701
- [25] Startsev E.A. and Lee W.W. 2014 *Phys. Plasmas* **21** 022505
- [26] Scott B.D. 2007 *Plasma Phys. Control. Fusion* **49** S25
- [27] LeBlanc B.P. et al 2001 *AIP Conf. Proc.* **595** 51
- [28] Smith D.R. et al 2008 *Rev. Sci. Instrum.* **79** 123501
- [29] Ruiz Ruiz J. 2015 *Phys. Plasmas* **22** 122501
- [30] Ren Y. et al 2014 *Experimental Observation of Nonlocal Electron Thermal Transport in NSTX RF-heated L-mode plasmas 25th IAEA fusion Energy Conf. (St. Petersburg, Russian Federation, 13–18 October 2014)* [EX/P6-43] ([http://www.naweb.iaea.org/napc/physics/FEC/FEC2014/fec2014-preprints/506\\_EXP643.pdf](http://www.naweb.iaea.org/napc/physics/FEC/FEC2014/fec2014-preprints/506_EXP643.pdf))
- [31] Wang W.X. et al 2007 *Phys. Plasmas* **14** 072306
- [32] Kotschenreuther M. et al 1995 *Comput. Phys. Commun.* **88** 128
- [33] Waltz R.E. and Miller R.L. 1999 *Phys. Plasmas* **6** 4265
- [34] Bell R.E. 2006 *Rev. Sci. Instrum.* **77** 10E902
- [35] Candy J. and Waltz R.E. 2003 *Phys. Rev. Lett.* **91** 045001
- [36] Sarazin Y. et al 2010 *Nucl. Fusion* **50** 054004
- [37] Idomura Y. et al 2009 *Nucl. Fusion* **49** 065029
- [38] Ku S. et al 2009 *Nucl. Fusion* **49** 115021
- [39] Heikinen J. et al 2008 *J. Comput. Phys.* **227** 5582
- [40] Rath F. et al 2016 *Phys. Plasmas* **23** 052309
- [41] Peeters A.G. et al 2016 *Phys. Plasmas* **23** 082517
- [42] Weikl A. et al 2017 *Phys. Plasmas* **24** 102317
- [43] Idomura Y. and Nakata M. 2014 *Phys. Plasmas* **21** 020706
- [44] Dif-Pradalier G. et al 2010 *Phys. Rev. E* **82** 025401
- [45] Dif-Pradalier G. et al 2015 *Phys. Rev. Lett.* **114** 085004
- [46] Dif-Pradalier G. et al 2017 *Nucl. Fusion* **57** 066026
- [47] Korpilo T. et al 2016 *Comput. Phys. Commun.* **203** 128
- [48] Howard N. et al 2016 *Nucl. Fusion* **56** 014004
- [49] Maeyama S. et al 2015 *Phys. Rev. Lett.* **114** 255002
- [50] Houlberg W.A. et al 1997 *Phys. Plasmas* **4** 3230
- [51] Kaye S.M. et al 2007 *Nucl. Fusion* **47** 499
- [52] Menard J. et al 2011 *IEEE/NPSS 24th Symp. on Fusion Engineering (Chicago, IL, 26–30 June 2011)* pp 1–8